

Contents lists available at ScienceDirect

# Heliyon

journal homepage: www.cell.com/heliyon



#### Research article



# Thermal stability analysis of nitrile additives in LiFSI for lithium-ion batteries: An accelerating rate calorimetry study

Mukarram Ali <sup>a,b,1</sup>, Siyoung Park <sup>c,1</sup>, Asif Raza <sup>a,b</sup>, Cheolhee Han <sup>c</sup>, Hyobin Lee <sup>c</sup>, Hochun Lee <sup>c</sup>, Yongmin Lee <sup>c,d,\*\*</sup>, Chilhoon Doh <sup>a,b,\*</sup>

- <sup>a</sup> Next Generation Battery Research Center, Korea Electrotechnology Research Institute (KERI), Changwon, 51543, Republic of Korea
- b Department of Electric Materials (Electro-Functional) Engineering, University of Science and Engineering (UST), Changwon, 51543, Republic of Korea
- <sup>c</sup> Department of Energy Science and Engineering, Daegu Gyeongbuk Institute of Science and Technology (DGIST), Daegu, 42988, Republic of Korea

#### ARTICLE INFO

# Keywords: Lithium-ion battery Thermal stability Accelerating rate calorimetry Nitrile additives Fire safety

#### ABSTRACT

Although lithium-ion batteries (LIBs) are extensively used as secondary storage energy devices, they also pose a significant fire and explosion hazard. Subsequently, thermal stability studies for LiPF6- and LiFSI-type electrolytes have been conducted extensively. However, the thermal characteristics of these electrolytes with thermally stable additives in a full cell assembly have yet to be explored. This study presents a comprehensive accelerating rate calorimetry (ARC) study. First, 1.2-Ah cells were prepared using a control commercial LiPF<sub>6</sub> electrolyte and LiFSI with a specific succinonitrile additive and ethyl-methyl carbonate as a thermally stable electrolyte additive. The kinetic parameters involved in heat generation and their effects on the thermal properties of the ARC module were analyzed from the heat-wait-seek (HWS), self-heating (SH), and thermal runaway (TR) stages. The results indicate that the addition of a succinonitrile additive to the LiFSI electrolyte lowers the decomposition temperatures of the solid electrolyte interface (SEI) owing to polymerization with Li at the anode, while simultaneously increasing the activation energy of reaction temperatures at SEI between the separator and the electrolyte. The maximum thermal-runaway temperature decreased from 417 °C ( $\Delta H = 5.26$  kJ) (LiPF<sub>6</sub>) to 285 °C  $(\Delta H = 2.068 \text{ kJ})$  (LiFSI + succinonitrile). This study provides key insights to the thermal characteristics of LiPF<sub>6</sub> and LiFSI during the self-heating and thermal runaway stages and indicates a practical method for achieving thermally stable LIBs.

# 1. Introduction

Lithium-ion batteries (LIBs) have emerged as ideal candidates for application as secondary storage energy devices in consumer electronics, electric vehicles (EVs), and electrochemical energy storage systems (ESS) [1,2]. Their high energy density, long life span, and zero-carbon emission (during operation) have made them front-runners for achieving the green technology era [3]. However, LIBs

<sup>&</sup>lt;sup>d</sup> Department of Chemical and Biomolecular Engineering, Yonsei University, Seoul 03722, Republic of Korea

<sup>\*</sup> Corresponding author. Next Generation Battery Research Center, Korea Electrotechnology Research Institute (KERI), 12, Jeongiui-gil, Seongsangu, Changwon, 51543, Republic of Korea.

<sup>\*\*</sup> Corresponding author. Department of Chemical and Biomolecular Engineering, Yonsei University, Seoul, 03722, Republic of Korea *E-mail addresses*: yongmin@yonsei.ac.kr (Y. Lee), chdoh@keri.re.kr (C. Doh).

<sup>&</sup>lt;sup>1</sup> These authors contributed equally to this work and are considered co-first authors.

pose a significant hazard because their electrolytes exhibit thermal runaway ( $T_{\rm tr}$ ), which can result in explosions [4]. Typically, a battery bed of an EV consists of several hundreds of cells connected in the form of a module. Therefore, the  $T_{\rm tr}$  of a single LIB can generate large amounts of heat, raising the temperature of neighboring cells and potentially causing a chain reaction [5,6]. Accidents resulting from the fires and explosions of LIBs are not uncommon, especially those involving cell phones, laptops, and EVs. Recently, fires and explosions involving the batteries of Samsung Note 7 (2017) [7], Hyundai KONA EV (2022) [8], and Tesla Model S (2023) [9] further highlight the safety risk associated with the use of LIBs.

Both external (battery management system, pressure/temperature sensors, thermal insulations) and internal methods can be used to ensure battery safety [10-14]. However, external methods can increase the cost, and weight of the battery bed, leading to decreased performance, especially in challenging environments like those encountered by EVs. Conversely, internal protection mechanisms provide protection using chemical additives and solvents (Supplementary Table S1). As most fire incidents originate from internal material failures rather than external causes, internal methods are often more effective in ensuring battery safety. Strategies such as modification at the cathode/anode interface [12–19], thermally switchable current collectors [20], thermal shutdown separators [21, 22], multifunctional electrolytes [23], and flame-retardant electrolyte additives [24-30] can address these challenges. Presently, the most commonly utilized salt in electrolytes is lithium hexafluorophosphate (LiPF<sub>6</sub>) and the most commonly used carbonate solvents are ethylene carbonate (EC) and dimethyl carbonate (DMC). These components, however, pose safety risks because of their high volatility (LiPF<sub>6</sub>,  $T_{tr}$  < 180 °C) and flammability, which can lead to fires and explosions [31]. In the last 20 years, significant efforts have been made toward finding suitable compounds that can be used as LIB electrolytes. Lithium imide salts have emerged as the best alternative. Lithium bis(trifluoromethanesulfonyl)imide (LiTFSI) is known for its good conductivity and thermal stability (LiTFSI,  $T_{tr}$ > 210 °C) [31–33]. However, it forms a stable soluble Al salt and fails to safeguard the aluminum current collector above 3.5 V [34]. Recently, bis(fluorosulfonyl) imide, Li[(FSO<sub>2</sub>)<sub>2</sub>N] (LiFSI, T<sub>tr</sub> > 200 °C), an imide family member, is attracting increasing interest, particularly for use as liquid electrolytes. This interest is driven by its well-defined properties, including no emission of hydrogen fluoride, low viscosity, high conductivity (>5 mS cm<sup>-1</sup>), and outstanding performance at both low and high temperatures, even under high rate conditions [35–39].

Thermal runaway arises when an exothermic reaction in an LIB spirals out of control. When the battery temperature surpasses 90 °C, the exothermic chemical reaction rate within the battery escalates, which further increases the cell temperature (self-heating stage, SHS) leading to thermal runaway (TRS) [40,41]. Shutdown separators are commonly used as a fail-safe method but these separators are often ineffective against thermal runaway due to melting of the separator >100 °C [4]. To address this issue, it is often recommended to use commercially viable flame-retardant additives. These additives function either chemically or physically in both condensed and vapor phases, thereby disrupting the combustion process during heating, pyrolysis, ignition, or flame spread [42,43]. Some recent studies have advocated the use of several nitrile-based additives in LIB electrolytes for suppressing the thermal runaway of LIB cells [26-30,44-47]. Succinonitrile (SN, NC-CH<sub>2</sub>-CH<sub>2</sub>-CN), a representative molecular non-ionic plastic crystal that shows plastic behavior at high temperatures, is attracting increasing interest because it exhibits high boiling point (267 °C) with negligible vapor pressure, and has lower flammability at high temperatures. In 2016, Liu et al. [48] reported an SN-based plastic crystal polymer electrolyte (CPLC-CPE) with SiO<sub>2</sub> particles connected with trimethylolpropane propoxylate triacrylate (TPPTA) that is thermally stable up to 230 °C. Similarly, in 2017, Zhang et al. [31] reported an SN-based electrolyte that increases the thermal stability of LIBs to up to 220 °C owing to the formation of a strong solid electrolyte interphase with the Li metal. More recently, 1,1,2,2-tetrafluoroethyl-2, 2,3,3-tetrafluoropropyl ether (TFE) has been proposed as a co-solvent for LiPF<sub>6</sub> along with FEC, EC, and DMC. TF50E showed high oxidative stability with Li metal to up to 5.5 V and high rate performance at 4.9 V [49]. In 2021, Gu et al. [50] used TFE with LiPF<sub>6</sub> and reported high capacity retention (87.1 %) with a graphite anode at an elevated temperature of 60 °C. Similarly, in 2023, Kim et al. [51] used TFE as an electrolyte additive with LiPF<sub>6</sub> and reported high capacity retention (70.9 %) against the SiO<sub>x</sub> anode. Ekeren et al. reported on the flame retardation property of TFE using the LiFSI electrolyte [52]. They showed that glass fibers soaked with the TFE/triethyl phosphate (TEP)-based LiFSI electrolyte solution appeared to be non-flammable, even when these fibers were repeatedly exposed to the butane flame. While numerous studies have examined the synthesis and performance effect of these additives in LIBs, a deeper exploration into their kinetic parameters and the fundamental causes of  $T_{\rm tr}$  in commercial cells has still not been performed. While differential scanning calorimetry and micro-calorimetry (C80) can be used to obtain insights at the material level, accelerating rate calorimetry (ARC) is more effective in providing a broader perspective by revealing key physical parameters that influence the module-level performance in the charged state of LIBs.

This study conducts a detailed investigation of the kinetic parameters of heat generation and determines the impact of SN additive on the thermal properties of LIBs across three distinct stages: the heat-wait-seek (HWS), self-heating (SHS), and TRS. This study concluded that the addition of SN in LiFSI increases the thermal stability of LIBs and provides a viable alternative for  $LiPF_6$  based electrolytes.

# 2. Experimental

#### 2.1. Preparation of LIBs

The 1.2-Ah (553,566) LIB cell (33.5  $\times$  64.5  $\times$  5.25 mm) was provided by U&S Energy (Korea). The cell contained a Li (Ni<sub>0.8</sub>Mn<sub>0.1</sub>Co<sub>0.1</sub>)O<sub>2</sub> (NMC811) cathode (positive electrode) and a 100 % graphite anode (negative electrode). The areal capacity of the NCM811 cathode was 2.7 mAh.cm<sup>-2</sup>, while that of the graphite anode was 2.9 mAh.cm<sup>-2</sup>. The nominal voltage was 3.77 V, and the nominal capacity was approximately 1200 mAh. Electrolytes of two different compositions were used. The base cell comprised 1-M LiPF<sub>6</sub> electrolyte with EC:EMC (1:2 v/v) (B-cell). The nitrile cell comprised 1-M LiFSI electrolyte with SN:TFE (5:1 mol%) and 5 wt

% FEC (N-cell), as reported previously [31,48]. Three formation cycles were conducted with constant current/constant voltage (CC/CV) charge. The CC discharge was 0.2C rate within 2.7–4.2 V. For ARC tests, 100 % state of charge was selected because most of the cells with  $T_{\rm tr}$  were usually in the charged state. The initial discharge capacities of the B-cell and N-cell are 1.17 and 1.14 Ah, respectively (Supplementary Figure S1). The physical and chemical characteristics of LIBs are listed in Supplementary Table S2.

#### 2.2. EV-ARC experiment details

The ARC experiments were conducted using extended volume–accelerating rate calorimetry (EV–ARC; Thermal Hazard Technology) (Fig. 1a). To obtain the most accurate results in accordance with the heat-transfer effect as reported previously [40], an in-house ARC chamber was designed (Fig. 1b and c). In order to maintain the temperature control accuracy and heat transfer effect the ARC was calibrated before the experiment (see Fig. S2). This ARC chamber was cylindrical and made of martensitic stainless steel. The chamber was 43 cm tall with an outer diameter of 21 cm and an inner diameter of 17 cm. The bottom ( $T_{\rm bm}$ ), top ( $T_{\rm top}$ ), and side ( $T_{\rm side}$ ) wall temperatures were measured by using n-type thermocouples connected to the ARC chamber. One n-type thermocouple was connected to the in-house EV–ARC chamber for accurately measuring the temperature ( $T_{\rm crc}$ ). Another n-type thermocouple was connected to an LIB to measure the cell-surface temperature ( $T_{\rm sam}$ ). The thermocouples of the ARC were annealed prior to the experiment for better accuracy. Thermo-electric annealing method was used for calibration of the thermocouples. The thermocouples were annealed at 350 °C for 4 h. The temperature at the cell tab can be different to cell surface temperature. So in this study only cell surface temperature was used at open circuit. Fig. 2 depicts the ARC chamber, experimental assembly, and images of the LIB cells after the tests.

Initially, the experiment followed the HWS stage. The LIB cell was preheated to 20 °C. The HWS stage began after 20 °C with 60 min of rest time and a sensitivity rate of 0.02 °C/min. During this period, if no self-heating was detected, then the temperature was increased by 5 °C in a stepwise manner. The temperature of the LIB was increased upon heating using an EV–ARC module. The self-heating reaction, which includes the decomposition of the SEI layer, anode/cathode material, and the electrolyte, did not begin in this stage. As soon as the rate of heating reached 0.02 °C/min, the ARC shifted to the SHS. During the SHS, the EV–ARC controls the LIB temperature ( $T_{\rm tr}$  %diff.  $\leq$  4 %,  $T_{\rm sam}/T_{\rm crc}$ ). During the SHS stage, the temperature increased by 0.5 °C/min after every 30 s till the decomposition reaction was complete and then by 1 °C/min till the TRS was achieved.

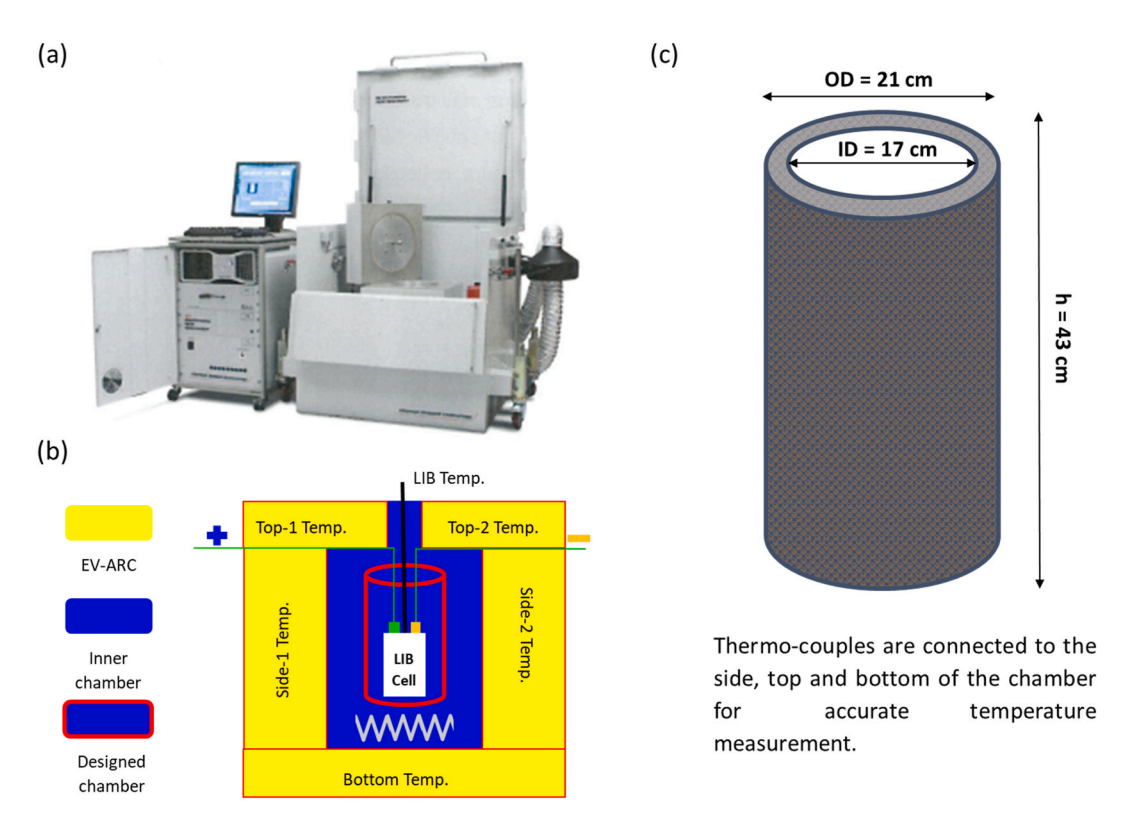


Fig. 1. (a) Image of an EV-ARC machine. (b) Schematic illustration of temperature and voltage measurement (EV-ARC chamber has an in-house chamber module). (c) Schematic illustration of the in-house ARC chamber.

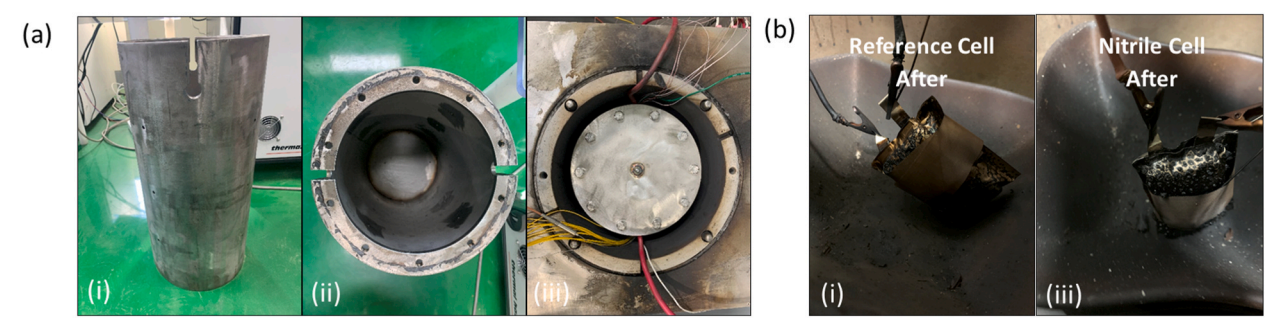


Fig. 2. (a) Digital images (i and ii) of the in-house EV-ARC module. (iii) Digital image of the in-house ARC module when connected with sample cells and thermocouples during the experiment. (b) Digital images of B-cell and N-cell after thermal runaway.

# 2.3. Evaluation of reaction kinetics

To evaluate the reaction kinetics, the temperature change in the SHS was measured. The cell temperature increases intrinsically during the SHS. This temperature rise in the adiabatic environment of the ARC test can be determined as reported previously [40,53]. As the temperature rise is intrinsic, the bulk activation energy  $(E_a)$  of the SHS can be calculated using Eqn. (1).

$$ln\frac{dT}{dt} \approx ln(\Delta T_{ad} A_i) - \left(\frac{E_a}{k_b T}\right)$$
 (1)

where  $\Delta T_{\rm ad}$  is the adiabatic temperature change,  $A_{\rm i}$  is the pre-exponential factor,  $E_{\rm a}$  is the activation energy,  $k_{\rm b}$  is the Boltzmann constant, and T is the reaction temperature in kelvin.  $E_{\rm a}$  can be obtained from the slope of the fitting curve using a  $\ln(dT/dt)$  vs 1/T plot.

The maximum self-heating rate  $(dT/dt)_{max}$ , internal short circuit temperature ( $T_{sct}$ ), and maximum thermal-runaway temperature ( $T_{max}$ ) can be evaluated from the temperature/temperature rate vs time/voltage plot (Fig. 3).

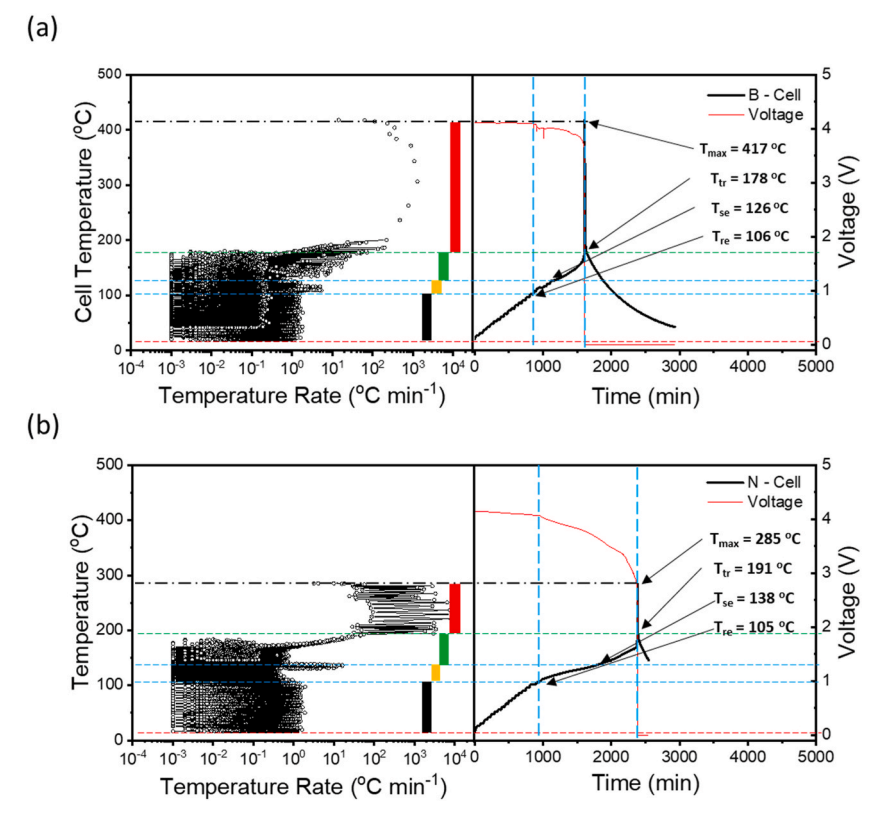


Fig. 3. (a, b) Temperature/temperature rate vs time/voltage plots for B-cell and N-cell. Black bar: HWS zone; yellow bar: reaction zone; green bar: SHS zone; and red bar: TRS zone.

# 2.4. Evaluation of thermokinetic parameters

The heat of reaction  $(\partial H)$  and the total heat of reaction  $(\Delta H)$  for the LIB cells were calculated using Eqs. (2) and (3).

$$\partial \mathbf{H} = C_p \left( T_{max} - T_{tr} \right) \tag{2}$$

$$\Delta H = m_c C_p (T_{max} - T_{tr}) \tag{3}$$

where  $m_c$  is the mass of the LIB cell and  $C_p$  is the total heat capacity for the sample LIB. A previous study reported a  $C_p$  of approximately 1 J/gK, as measured by using the EV–ARC module [54]. Notably, there is some overlapping of the exothermic reactions in certain temperature ranges (Fig. 3). The exact temperature ranges for the decomposition of the SEI layer, anode, cathode, and electrolyte and other remaining materials, including the binder, depend on battery specifications. However, this study investigated bulk parameters, because most of the reaction propagation during TRS is abrupt and generally depends on the electrolyte decomposition, gas

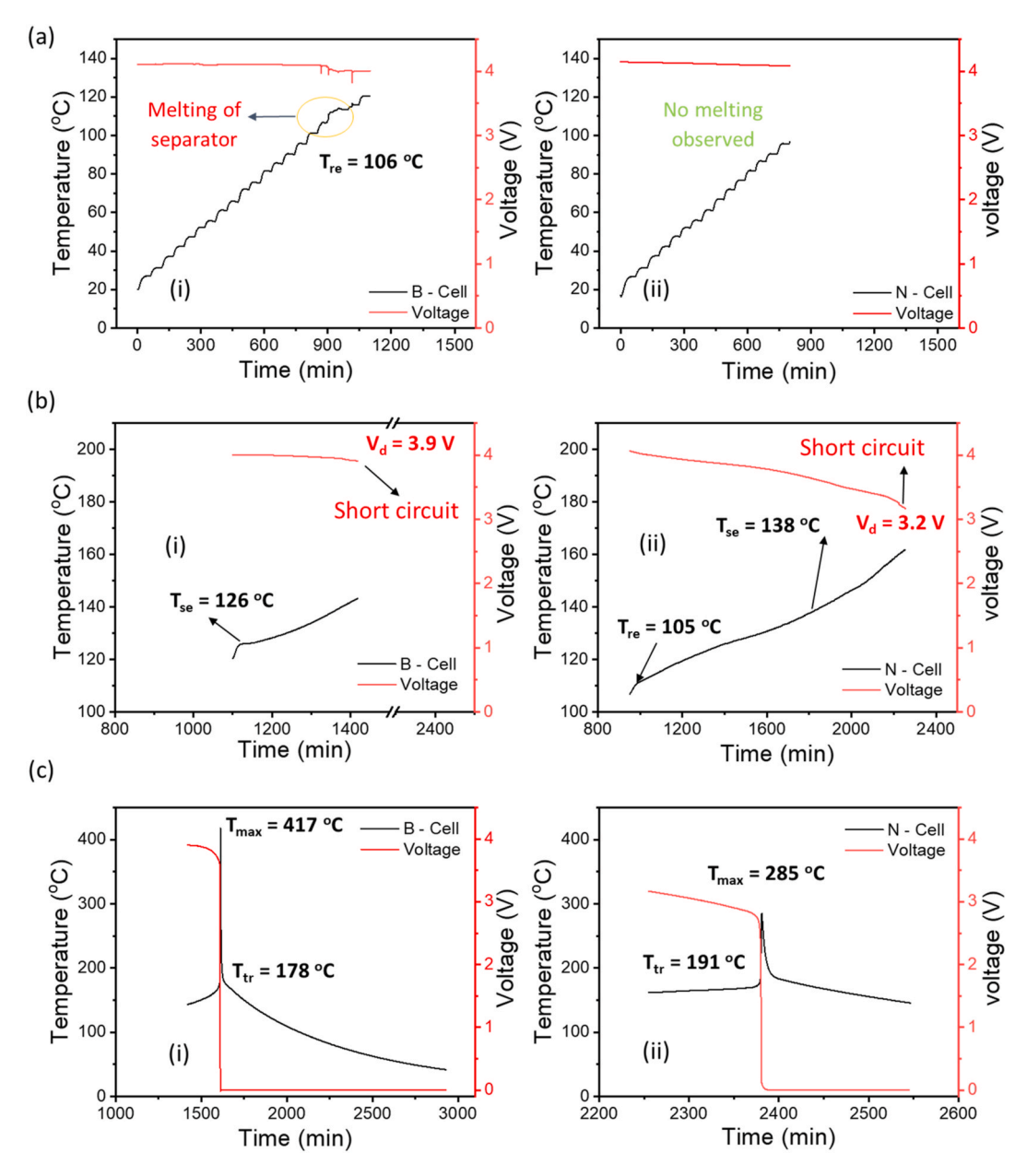


Fig. 4. Time vs voltage plots for (a) HWS zone in (i) B-cell and (ii) N-cell. (b) SHS zone in (i) B-cell and (ii) N-cell. (c) TRS zone in (i) B-cell and (ii) N-cell.

propagation, and parasitic reactions.

#### 2.5. Simulation study

To study the thermal behavior of LIBs more systematically during the SHS, a three-dimensional (3D) thermal simulation was conducted in COMSOL Multiphysics 6.1 (Supplementary Fig. S3). The  $T_{\rm sam}$  and  $T_{\rm crc}$  experimental data were directly used to determine the simulation temperature. The heat source was calculated by using the IPOPT method via a gradient-based optimization solver. The thermal simulation was performed during the entire SHS period of each cell to determine the thermal propagation inside the cell and heat flux from the cell surface to the air. The results obtained were used to indicate the actual structures of the ARC and pouch cell. The thermal physical properties of this model are listed in Supplementary Table S3.

#### 3. Results and discussion

Supplementary Figs. S4 and S5 plots the change in the temperatures of B-cell and N-cell ( $T_{\rm sam}$ ) with that of the crucible ( $T_{\rm crc}$ ) during the ARC experiment. Both  $T_{\rm sam}$  and  $T_{\rm crc}$  are similar throughout the ARC test. The %error for  $T_{\rm cm}/T_{\rm max}$  is  $\leq 1$  % for both B-cell and N-cell. Interestingly, when compared with the side, bottom and top temperatures, the %error increases up to  $\geq 15$  %. This shows the effectiveness of the designed ARC module during temperature measurement. Normally, during thermal runaway, the ARC cannot maintain the wall temperature and the difference between the cell temperature and the wall temperature exceeds 400 °C [40]. This difference depends on the aggressive decomposition reaction rate and may further cause the internal temperature difference within the sample, which in turn increases the uncertainty for kinetics estimation. Therefore, the uncertainty of the heat of reaction greatly depends on the external temperature difference. In this study, the difference between the crucible temperature and the cell temperature is < 15 °C at  $T_{\rm max}$ , which signifies the accuracy of temperature measurement (by using the crucible) by minimizing the external heat-transfer effect.

# 3.1. HWS stage

During the HWS stage in this study (Fig. 4a (i-ii)), the cell was externally heated gradually in 5-°C steps. As soon as the cell surface exceeds this temperature, the ARC stops heating. It begins the next interval of heating after a waiting period of 60 min. Once the thermal equilibrium is reached during the waiting period, the system enters the seek period that lasts 10 min. In the seek-period, the self-heating rate of the cell is monitored by tracking the rise in cell temperature. During the HWS stage, a negligible external temperature difference of < 0.01 °C between  $T_{\rm crc}$  and  $T_{\rm sam}$  was observed, indicating that a well-maintained adiabatic condition. The interval at which the ARC detects a larger value than the exothermic sensitivity (0.02 °C/min) is considered the time at which the onset temperature (T<sub>re</sub>) is achieved. The HWS stage is studied for both the B-cell and N-cell. For the B-cell, a sudden drop in voltage (internal short circuit) was observed at 106 °C (Tre), which was accompanied along with an abrupt temperature change (Fig. 4a (i-ii)). This temperature is considered to represent the reaction temperature for the interaction between the electrolyte and the separator interface [4]. The melting of the separator is an exothermic reaction, which triggers the SHS. We can clarify this phenomenon by using LiPF<sub>6</sub> with EC and DMC as co-solvents. Under such a condition, the reaction between the separator and the SE interface directly begins at approximately 85 °C, forming LiF and PF<sub>5</sub> as by-products [55]. As PF<sub>5</sub> (Lewis acid) is highly acidic, it further reacts with the SEI to form gas vapors. As a result, the self-heating rate abruptly increases, as can be observed in Fig. 3a. When EMC is added to LiPF<sub>6</sub>, stable Li<sub>2</sub>CO<sub>3</sub> is formed in addition to PF<sub>5</sub> on the cathode interface, which decreases the self-heating rate. However, the formation of Li<sub>2</sub>CO<sub>3</sub> results in the formation of cracks at the cathode interface at high temperatures or high currents, which may lead to an internal short circuit and abrupt exothermic reactions [56]. Interestingly, no melting of the separator was observed in the case of the N-cell, which indicates the chemical inertness of the SN in LiFSI with the commercial separator. The addition of TFE also inhibits the exothermic reaction of LFSI with commercial separators [52].

The reaction temperature for the N-cell was observed to be 105 °C ( $T_{\rm re}$ ), as seen in Fig. 3b. This reaction temperature is characteristic of imide salts, which are used as electrolytes with graphite anodes [36,37,57]. Moreover, in imide-based electrolytes, it is not the internal short circuit that triggers the SHS; instead, the SHS is a result of the exothermic reaction between the imide-based electrolytes and the SEI of electrodes [36]. However, it is important to note that because of the flame inertness of TFE and because it exhibits good wettability with the separator, no rise in the heating rate was observed, in contrast to that observed with the B-cell. Further studies related to the SEI stability of TFE and SN with various cathode materials and Li metal/graphite anodes may provide greater insight into this behavior.

# 3.2. SHS

The SHS in LIBs involves heat transfer. In this stage, the ARC controls the crucible temperature so that it matches the cell-surface temperature. The difference between  $T_{\rm crc}$  and  $T_{\rm sam}$  is small because of better heat transfer between the crucible and the sample. Hence, it is easy to quantify thermal parameters. Any increase in the cell temperature at this stage is caused by self-heating owing to exothermic reactions occurring within the cell rather than by external heating by the ARC [40]. Some examples of these exothermic reactions mainly include the decomposition of the SEI and electrolytes, which generate a large amount of gases until the thermal runaway is observed. The released oxygen and heat at the SHS complete the combustion triangle required for inducing and maintaining fire in organic electrolytes, leading to an explosion hazard.

Fig. 4b (i–ii) shows the SHS of the B-cell and N-cell. A sharp increase in the temperature was observed, denoted as T<sub>SP</sub>. The T<sub>SP</sub> values of the B-cell and N-cell were measured to be 126 and 138 °C, respectively (Fig. 4b). These temperatures indicate the heat generated by the SEI and electrolyte decomposition in these cells. As the  $T_{\rm se}$  of the N-cell was higher than that of the B-cell, it can be suggested that the use of SN in LiFSI affords thermal stability to the cell. The decrease in  $T_{\rm SE}$  is attributed to the reduction in the generation of gas owing to the reduced generation of internal heat in the cell [25,30,46]. The increase in the SEI-decomposition temperature of the N-cell is attributed to the reaction between the intercalated Li in graphite anode and LiFSI, as previously reported [38]. In the case of the B-cell, the SEI decomposition began at a low temperature of 126 °C, because of the formation of PF<sub>5</sub> and a fast parasitic reaction with the SEI of the anode [56]. This stage is indicated by a sharp hump in Fig. 4b (i). Moreover, the maximum self-heating rates for the B-cell and N-cell were 26,171 and 8143 °C min<sup>-1</sup>, respectively (Table S4). This result shows a 60 % reduction in the maximum self-heating rate for the N-cell, emphasizing the role of SN and LiFSI in imparting thermal stability to the N-cell. Normally, when the SEI begins to decompose at the anode and cathode interface, the internal short circuit resulting from the decomposition of the separator increases the number of parasitic reactions in conventional LiPF<sub>6</sub> electrolyte systems. The oxygen released at the cathode and sudden delithiation at the graphite anode cause a chain reaction, releasing a large amount of heat. Thus, the self-heating rate rapidly increases, ultimately causing thermal runaway in the cells. The LiFSI also shows a similar mechanism. However, because of the introduction of the SN additive in the N-cell, the interfacial resistance at the anode increases owing to the polymerization of the Li metal with nitriles, which in turn increases the SEI stability to up to 120 °C [31]. In addition, high oxidative stability was observed when TFE was used with the SN at cathode [49]. Hence, TFE acts as a passivating agent for oxygen generation from the cathode, which increases the SEI-decomposition temperature to up to 138 °C and decreases the self-heating rate. Fig. 5 shows the  $\ln(dT/dt)$  vs 1/T plot for both the B-cell and N-cell. The E<sub>a</sub> values were 291 and 405 kJ mol<sup>-1</sup> for the B-cell and N-cell, respectively. A minor non-linear behavior is observed between 2.23 and 2.25 1000/K on x-axis in Fig. 5b, which can be attributed towards the polymerization of LiFSI with SN. The SHS temperature in LiFSI cell is dependent on the rate at which the internal temperature increase intrinsically. However, the polymerization of LiFSI with SN slows down this behavior and the temperature increase dulls down, hence a minor non-linear patches can occur. However, further detailed study of SN and LFSI behavior at elevated temperatures is needed to this phenomenon. It is apparent that the introduction of SN along with LiFSI increases the reaction activation energy, which in turn increases the thermal stability at high temperatures (>90 °C). Moreover, the increase in Ea also increases the temperature at which the SHS stage is achieved, which results in a slow increase in the temperature. Consequently, the maximum thermal runaway rate is decreased.

# 3.3. TRS

As soon as the thermal-runaway temperature is reached, a sharp voltage drop ( $V_d$ ) due to a complete internal short circuit is observed in all cells, including both the B-cell and N-cell. Importantly,  $V_d$  drops of 0.3 and 1.0 V were observed for the B-cell and N-cell, respectively (Fig. 4c). The increase in the  $V_d$  of the N-cell can be attributed to the polymerization reaction of the intercalated Li with the nitriles from the SN additive. The more the voltage drop occurs before thermal runaway, the smaller the energy release will be owing to the accumulated potential energy. After 307 min of SHS,  $T_{\rm tr}$  became 191 °C in case of the B-cell, while it was only 178 °C for the N-cell even after 1305 min of SHS. Hence, it can be suggested that adding the SN additive to LiFSI slows down the thermal runaway compared to that achieved by using EMC with LiPF<sub>6</sub> because of the increase in the  $E_a$  of the N-cell. The specific cause of this increase in  $E_a$  is difficult to quantize in this study as the anode/cathode/separator interfaces have different compositions. However, future studies considering the characterization of SEI formation during thermal runaway can provide further insights concerning the stability of SN in LiFSI. The maximum thermal-runaway temperatures ( $T_{\rm max}$ ) for the B-cell and N-cell are 417 and 285 °C, respectively. This decrease in  $T_{\rm max}$  reduces the total heat of reaction to 5.26 and 2.07 kJ for the B-cell and N-cell, respectively. Hou et al. [36] showed that most of the heat released during thermal runaway is caused by the decomposition of the electrolyte itself. The thermal runaway of the cathode and

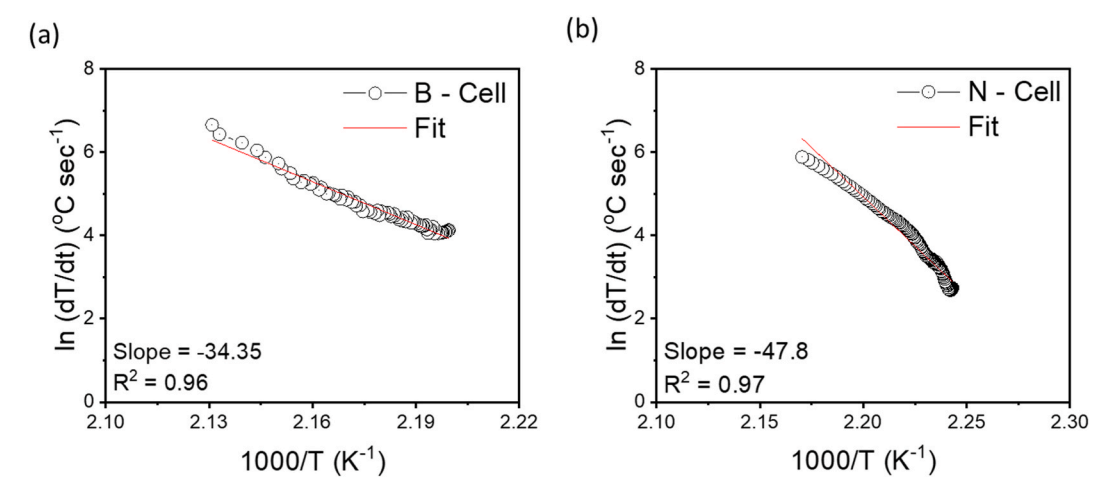


**Fig. 5.** In (dT/dt) vs 1000/T plots for **(a)** B-cell and **(b)** N-cell. The plots were linearly fit with a goodness of fit of ≈0.96.

anode each produced only 1/10th of the total heat. In case of the B-cell, the exponential growth of dT/dt (26,171 °C min<sup>-1</sup>) with temperature is attributed to extensive exothermic chemical reactions, caused mainly by PF<sub>5</sub> formation and oxidation at the cathode. That is, multiple reactions occurred between the anode/cathode and the electrolyte, initiated in a sequential manner as the temperature increased. The heat released by these reactions led to a continuous increase in the temperature of the full cell. This shows that SN additives in the N-cell slowed down the decomposition reaction rate of LiFSI during the SHS, leading to decreased dT/dt (8143 °C min<sup>-1</sup>) and reduced heat of reaction during thermal runaway, thereby mitigating the risk of high-energy explosions.

#### 3.4. Simulation analysis for heat generation during SHS till thermal runaway

Thermal simulation is a useful methodology to estimate the thermal behavior of each cell inside the ARC chamber. First, the 3D structures of the ARC chamber, the in-house chamber, and the internal structure of the pouch cell in this study were digitally obtained to show thermal propagation or specific heat generation within cells (Supplementary Fig. S6). This thermal simulation aims to replicate the real experimental situations, mirroring not only the 3D digital structure but also temperature changes of cells, enabling accurate calculation of heat propagation and generation in cells.

We simulated the SHS because the SHS is a period when cells exhibit important thermal behaviors that depend on the additives used before the thermal runaway is reached (i.e., Fig. 4b). During the SHS period,  $T_{\text{sam}}$  and  $T_{\text{crc}}$  of the in-house chamber were used as simulation settings. The heat source from the stack's domain was calculated by using these experimental data, Fig. 6 shows both experimental (dashed line) and simulation results (solid line) for 469 min for the B-cell and for 1412 min for the N-cell, respectively. Additionally, the 3D temperature gradient images of each cell well matched with the initial, middle, and final states during the SHS period. The red solid line indicates the maximum temperature that the cell can reach, while the blue solid line indicates the average temperature of the cells. The average simulation temperatures are slightly higher than the experimental values throughout the SHS period, which implies that the internal temperature of the cell is slightly higher than that of the pouch surface. Next, heat generated by each cell during the SHS was estimated. The heat generated during the SHS region varies significantly depending on the type of electrolyte used (Supplementary Fig. S6). This behavior is also evident by the temperature rise per minute shown in Fig. 4b. The average of the total heat source for each cell is as follows: 0.035 W (B-cell) and 0.012 W (N-cell). A sharp increase in heat generation was calculated at the end of SHS, indicating a rapid temperature rise that triggered the thermal runaway. The N-cell showed a 65 % reduction in heat generation compared to that demonstrated by the B-cell, which is in accordance with the experimental results, as discussed previously. Supplementary Fig. S6 shows that in the B-cell, heat generation began progressively after 350 min (start of internal reactions) because of the decomposition of the separator and anode SEI. However, this progressive heat generation was not observed in the N-cell. However, after 1100 min, a small increase in heat generation was observed in the N-cell. However, it normalizes because of the polymerization of Li with SN at the anode SEI, leading to the suppression of further decomposition. Furthermore, the heat flux from the pouch surface is almost negligible because the temperatures of the pouch surface and external air were controlled to be the same. Based on these simulation results, we can confirm that the SN-based LiFSI can effectively suppress heat generation, leading to a higher thermal-runaway temperature.

# 4. Conclusions

This study unearthed pivotal insights into the potential benefits of incorporating nitrile-based additives into the LiFSI electrolyte. A steep reduction in the decomposition temperatures of the SEI and a simultaneous increment in the activation energy were distinctly observed. A substantial mitigation in the maximum thermal-runaway temperature from a dangerous 417  $^{\circ}$ C to a considerably lower 285  $^{\circ}$ C was also observed. The enthalpy change ( $\Delta H$ ) concurrently decreased from 5.26 to 2.06 kJ, revealing a diminished energy

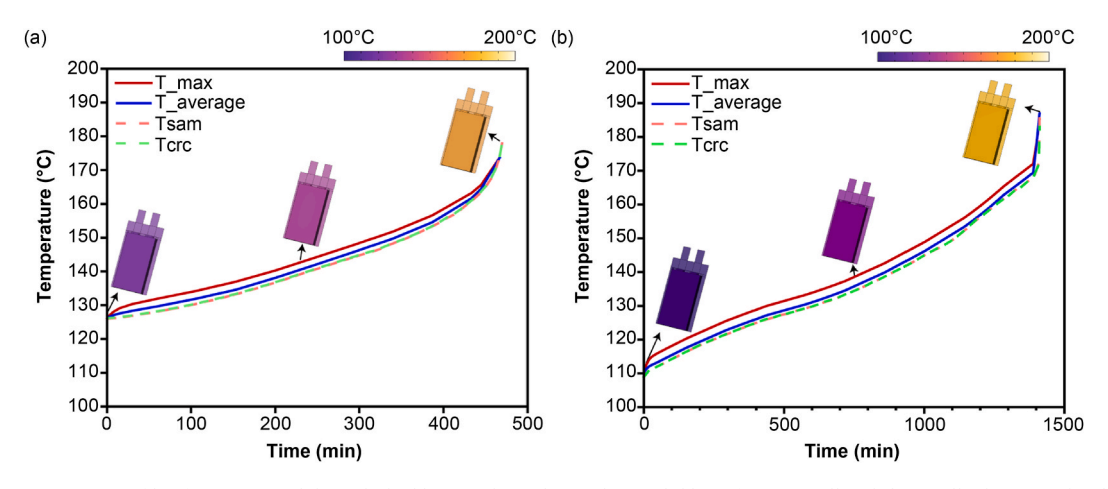


Fig. 6. Temperature profile of experimental data (dashed line) and simulation data (solid line) for (a) B-cell and (b) N-cell. Three pouch cell images of each graph represent the initial state, middle state, and final state of the SHS, respectively.

release during thermal runaway, thereby enhancing the intrinsic safety of LIBs. These findings indicate that LIBs containing SN-LiFSI electrolytes exhibit enhanced safety and performance, thereby laying the groundwork for more optimized energy storage systems. Moreover, future optimization and compositional studies of TFE and SN electrolyte additives may provide further insights towards achieving high thermal stability in LIBs.

# **Funding**

This study was supported by the program of UST Young Scientist+Research Program 2023 through the University of Science and Technology (grant number 22A03068) and Korea Electrotechnology Research Institute (KERI) Primary research program through the National Research Council of Science & Technology (NST) funded by the Ministry of Science and ICT (MSIT) (No. 24A01017), of the Republic of Korea. The funder had no role in the study design; in the collection, analysis, or interpretation of data; in the writing of the report; or in the decision to submit the article for publication.

# Data availability statement

Data included in article/supp. material/referenced in article.

# CRediT authorship contribution statement

Mukarram Ali: Writing – original draft, Investigation, Funding acquisition, Formal analysis, Data curation. Siyoung Park: Writing – original draft, Software, Investigation, Formal analysis, Data curation. Asif Raza: Writing – original draft, Formal analysis. Cheol-Hee Han: Writing – original draft, Software, Investigation, Formal analysis, Data curation. Hyo-Bin Lee: Writing – review & editing, Validation, Project administration, Methodology, Conceptualization. Ho-Cheon Lee: Writing – review & editing, Visualization, Validation, Supervision, Software, Resources, Project administration, Methodology, Conceptualization. Yong Min Lee: Visualization, Validation, Supervision, Software, Resources, Project administration, Methodology, Conceptualization. Chil-Hoon Doh: Writing – review & editing, Visualization, Validation, Supervision, Resources, Project administration, Methodology, Investigation, Funding acquisition, Formal analysis, Data curation, Conceptualization.

#### Declaration of competing interest

The authors declare that they have no known competing financial interests or personal relationships that could have appeared to influence the work reported in this paper.

# Acknowledgements

None.

# Appendix A. Supplementary data

Supplementary data to this article can be found online at https://doi.org/10.1016/j.heliyon.2024.e29397.

# References

- $[1] \ \ J.M. \ Tarascon, \ M. \ Armand, \ Building \ better \ batteries, \ Nature \ 451 \ (2008) \ 652, \ https://doi.org/10.1038/451652a.$
- [2] J.M. Tarascon, M. Armand, Issues and challenges facing rechargeable lithium batteries, Nature 414 (2001) 359, https://doi.org/10.1038/35104644.
- [3] Y.-G. Lee, S. Fujiki, C. Jung, N. Suzuki, N. Yashiro, R. Omoda, D.-S. Ko, T. Shiratsuchi, T. Sugimoto, S. Ryu, J.H. Ku, T. Watanabe, Y. Park, Y. Aihara, D. Im, I. T. Han, High-energy long-cycling all-solid-state lithium metal batteries enabled by silver–carbon composite anodes, Nat. Energy 5 (2020) 299, https://doi.org/10.1038/s41560-020-0575-z.
- [4] K. Liu, Y. Liu, D. Lin, A. Pei, Y. Cui, Materials for lithium-ion battery safety, Sci. Adv. 4 (2018) 4, https://doi.org/10.1126/sciadv.aas9820.
- [5] Q. Wang, P. Ping, X. Zhao, G. Chu, J. Sun, C. Chen, Thermal runaway caused fire and explosion of lithium ion battery, J. Power Sources 208 (2012) 210, https://doi.org/10.1016/j.jpowsour.2012.02.038.
- [6] T.M. Bandhauer, S. Garimella, T.F. Fuller, A critical review of thermal issues in lithium-ion batteries, J. Electrochem. Soc. 158 (2011) R1, https://doi.org/ 10.1149/1.3515880.
- [7] P. Mozur, Galaxy Note 7 fires caused by battery and design flaws, Samsung Says, New York Times (2017). https://www.nytimes.com/2017/01/22/business/samsung-galaxy-note-7-battery-fires-report.html.
- [8] M. Herh, Hyundai Motor's Kona EV catches fire while driving, Bus. Korea (2022). https://www.businesskorea.co.kr/news/articleView.html?idxno=85875.
- [9] G. Kay, See photos from the Tesla Model S that "spontaneously" caught fire while driving down the highway, Bus. Insid. (2023). https://www.businessinsider.com/tesla-model-s-battery-caught-fire-driving-highway-photos-2023-1.
- [10] G. Dong, M. Lin, Model-based thermal anomaly detection for lithium-ion batteries using multiple-model residual generation, J. Energy Storage 40 (2021) 102740, https://doi.org/10.1016/j.est.2021.102740.
- [11] X. Ling, Q. Zhang, Y. Xiang, J.S. Chen, X. Peng, X. Hu, A Cu/Ni alloy thin-film sensor integrated with current collector for in-situ monitoring of lithium-ion battery internal temperature by high-throughput selecting method, Int. J. Heat Mass Transf. 214 (2023) 124383, https://doi.org/10.1016/j.ijheatmasstransfer.2023.124383.

[12] Z. Li, J. Zhang, B. Wu, J. Huang, Z. Nie, Y. Sun, F. An, N. Wu, Examining temporal and spatial variations of internal temperature in large-format laminated battery with embedded thermocouples, J. Power Sources 241 (2013) 536, https://doi.org/10.1016/j.jpowsour.2013.04.117.

- [13] Z. Chen, J. Lin, C. Zhu, Q. Zhuang, Q. Chen, Y. Wei, S. Wang, D. Wu, Detection of jelly roll pressure evolution in large-format Li-ion batteries via in situ thin film flexible pressure sensors, J. Power Sources 566 (2023) 232960, https://doi.org/10.1016/j.jpowsour.2023.232960.
- [14] Y. Chen, Y. Kang, Y. Zhao, L. Wang, J. Liu, Y. Li, Z. Liang, X. He, X. Li, N. Tavajohi, B. Li, A review of lithium-ion battery safety concerns: the issues, strategies, and testing standards, J. Energy Chem. 59 (2021) 83, https://doi.org/10.1016/j.jechem.2020.10.017.
- [15] A. Raza, J.Y. Jung, C.H. Lee, B.G. Kim, J.H. Choi, M.S. Park, S.M. Lee, Swelling-controlled double-layered SiO<sub>x</sub>/Mg<sub>2</sub>SiO<sub>4</sub>/SiO<sub>x</sub> composite with enhanced initial Coulombic efficiency for lithium-ion battery, ACS Appl. Mater. Interfaces 13 (2021) 7161, https://doi.org/10.1021/acsami.0c19975.
- [16] K. Liu, A. Pei, H.R. Lee, B. Kong, N. Liu, D. Lin, Y. Liu, C. Liu, P. chun Hsu, Z. Bao, Y. Cui, Lithium metal anodes with an adaptive "solid-liquid" interfacial protective layer, J. Am. Chem. Soc. 139 (2017) 4815, https://doi.org/10.1021/jacs.6b13314.
- [17] G. Zheng, S.W. Lee, Z. Liang, H.W. Lee, K. Yan, H. Yao, H. Wang, W. Li, S. Chu, Y. Cui, Interconnected hollow carbon nanospheres for stable lithium metal anodes, Nat. Nanotechnol. 9 (2014) 618, https://doi.org/10.1038/nnano.2014.152.
- [18] Y. Wu, A. Manthiram, High capacity, surface-modified layered Li[Li<sub>(1-x)</sub>/3Mn<sub>(2-x)</sub>/3Ni<sub>x</sub>/3Co<sub>x</sub>/3]O<sub>2</sub> cathodes with low irreversible capacity loss, Electrochem. Solid State Lett. 9 (2006) 221. https://doi.org/10.1149/1.2180528.
- [19] L. Xia, S.L. Li, X.P. Ai, H.X. Yang, Y.L. Cao, Temperature-sensitive cathode materials for safer lithium-ion batteries, Energy Environ. Sci. 4 (2011) 2845, https://doi.org/10.1039/c0ee00590h.
- [20] Z. Chen, P.C. Hsu, J. Lopez, Y. Li, J.W.F. To, N. Liu, C. Wang, S.C. Andrews, J. Liu, Y. Cui, Z. Bao, Fast and reversible thermoresponsive polymer switching materials for safer batteries, Nat. Energy 1 (2016) 15009, https://doi.org/10.1038/nenergy.2015.9.
- [21] K. Liu, D. Zhuo, H.W. Lee, W. Liu, D. Lin, Y. Lu, Y. Cui, Extending the life of lithium-based rechargeable batteries by reaction of lithium dendrites with a novel silica nanoparticle sandwiched separator, Adv. Mater. 29 (2017) 1, https://doi.org/10.1002/adma.201603987.
- [22] M. Baginska, B.J. Blaiszik, R.J. Merriman, N.R. Sottos, J.S. Moore, S.R. White, Autonomic shutdown of lithium-ion batteries using thermoresponsive microspheres, Adv. Energy Mater. 2 (2012) 583, https://doi.org/10.1002/aenm.201100683.
- [23] J. Ding, T. Tian, Q. Meng, Z. Guo, W. Li, P. Zhang, F.T. Ciacchi, J. Huang, W. Yang, Smart multifunctional fluids for lithium ion batteries: enhanced rate performance and intrinsic mechanical protection, Sci. Rep. 3 (2013) 1, https://doi.org/10.1038/srep02485.
- [24] X. Wang, E. Yasukawa, S. Kasuya, Nonflammable trimethyl phosphate solvent-containing electrolytes for lithium-ion batteries: I. Fundamental properties, J. Electrochem. Soc. 148 (2001) A1058, https://doi.org/10.1149/1.1397773.
- [25] S.L. Guillot, M.L. Usrey, A. Peña-Hueso, B.M. Kerber, L. Zhou, P. Du, T. Johnson, Reduced gassing in lithium-ion batteries with organosilicon additives, J. Electrochem. Soc. 168 (2021) 030533, https://doi.org/10.1149/1945-7111/abed25.
- [26] H.J. Santner, K.C. Möller, J. Ivančo, M.G. Ramsey, F.P. Netzer, S. Yamaguchi, J.O. Besenhard, M. Winter, Acrylic acid nitrile, a film-forming electrolyte component for lithium-ion batteries, which belongs to the family of additives containing vinyl groups, J. Power Sources 119–121 (2003) 368, https://doi.org/10.1016/S0378-7753(03)00268-4.
- [27] L. Liu, W. Gao, Y. Cui, S. Chen, A bifunctional additive bi(4-flurorophenyl) sulfone for enhancing the stability and safety of nickel-rich cathode based cells, J. Allovs Compd. 820 (2020) 153069, https://doi.org/10.1016/j.jallcom.2019.153069.
- [28] Y.R. Kung, C.Y. Li, P. Hasin, C.H. Su, J.Y. Lin, Effects of butadiene sulfone as an electrolyte additive on the formation of solid electrolyte interphase in lithium-ion batteries based on Li<sub>4</sub>Ti<sub>5</sub>O<sub>12</sub> anode materials, Polymers 15 (2023) 1965, https://doi.org/10.3390/polym15081965.
- [29] C. Liao, B. Guo, X.G. Sun, S. Dai, Synergistic effects of mixing sulfone and ionic liquid as safe electrolytes for lithium sulfur batteries, ChemSusChem 8 (2015) 353, https://doi.org/10.1002/cssc.201402800.
- [30] X. Zheng, X. Wang, X. Cai, L. Xing, M. Xu, Y. Liao, X. Li, W. Li, Constructing a protective interface film on layered lithium-rich cathode using an electrolyte additive with special molecule structure, ACS Appl. Mater. Interfaces 8 (2016) 30116, https://doi.org/10.1021/acsami.6b09554.
- [31] Q. Zhang, K. Liu, F. Ding, W. Li, X. Liu, J. Zhang, Safety-reinforced succinonitrile-based electrolyte with interfacial stability for high-performance lithium batteries, ACS Appl. Mater. Interfaces 9 (2017) 29820, https://doi.org/10.1021/acsami.7b09119.
- [32] V. Aravindan, J. Gnanaraj, S. Madhavi, H. Liu, Lithium-ion conducting electrolyte salts for lithium batteries, Chem. Eur J. 17 (2011) 14326, https://doi.org/10.1002/chem.201101486.
- [33] B. Pohl, M.M. Hiller, S.M. Seidel, M. Grünebaum, H.D. Wiemhöfer, Nitrile functionalized disiloxanes with dissolved LiTFSI as lithium ion electrolytes with high thermal and electrochemical stability, J. Power Sources 274 (2015) 629, https://doi.org/10.1016/j.jpowsour.2014.10.080.
- [34] B. Ziv, O. Haik, E. Zinigrad, M.D. Levi, D. Aurbach, I.C. Halalay, Investigation of graphite foil as current collector for positive electrodes of Li-ion batteries, J. Electrochem. Soc. 160 (2013) A581, https://doi.org/10.1149/2.034304jes.
- [35] K. Zaghib, P. Charest, A. Guerfi, J. Shim, M. Perrier, K. Striebel, Safe Li-ion polymer batteries for HEV applications, J. Power Sources 134 (2004) 124, https://doi.org/10.1016/j.jpowsour.2004.02.020.
- [36] J. Hou, L. Lu, L. Wang, A. Ohma, D. Ren, X. Feng, Y. Li, Y. Li, I. Ootani, X. Han, W. Ren, X. He, Y. Nitta, M. Ouyang, Thermal runaway of lithium-ion batteries employing LiN(SO<sub>2</sub>F)<sub>2</sub>-based concentrated electrolytes, Nat. Commun. 11 (2020) 5100, https://doi.org/10.1038/s41467-020-18868-w.
- [37] N. Ehteshami, A. Eguia-Barrio, I. de Meatza, W. Porcher, E. Paillard, Adiponitrile-based electrolytes for high voltage, graphite-based Li-ion battery, J. Power Sources 397 (2018) 52, https://doi.org/10.1016/j.jpowsour.2018.07.004.
- [38] G.G. Eshetu, S. Grugeon, G. Gachot, D. Mathiron, M. Armand, S. Laruelle, LiFSI vs. LiPF<sub>6</sub> electrolytes in contact with lithiated graphite: comparing thermal stabilities and identification of specific SEI-reinforcing additives, Electrochim. Acta 102 (2013) 133, https://doi.org/10.1016/j.electacta.2013.03.171.
- [39] D.R.L. Murali, F. Banihashemi, J.Y.S. Lin, Zeolite membrane separators for fire-safe Li-ion batteries effects of crystal shape and membrane pore structure, J. Memb. Sci. 680 (2023) 121743, https://doi.org/10.1016/j.memsci.2023.121743.
- [40] X. He, C. Zhao, Z. Hu, F. Restuccia, F. Richter, Q. Wang, G. Rein, Heat transfer effects on accelerating rate calorimetry of the thermal runaway of Lithium-ion batteries, Process Saf. Environ. Prot. 162 (2022) 684, https://doi.org/10.1016/j.psep.2022.04.028.
- [41] M. Henriksen, K. Vaagsaether, J. Lundberg, S. Forseth, D. Bjerketvedt, Explosion characteristics for Li-ion battery electrolytes at elevated temperatures, J. Hazard Mater. 371 (2019) 1, https://doi.org/10.1016/j.jhazmat.2019.02.108.
- [42] Y.E. Hyung, D.R. Vissers, K. Amine, Flame-retardant additives for lithium-ion batteries, J. Power Sources 119–121 (2003) 383, https://doi.org/10.1016/S0378-7753(03)00225-8.
- [43] E.R. Logan, J.R. Dahn, Electrolyte design for fast-charging Li-ion batteries, Trends Chem 2 (2020) 354, https://doi.org/10.1016/j.trechm.2020.01.011.
- [44] L. Xia, D. Wang, H. Yang, Y. Cao, X. Ai, An electrolyte additive for thermal shutdown protection of Li-ion batteries, Electrochem. Commun. 25 (2012) 98, https://doi.org/10.1016/j.elecom.2012.09.038.
- [45] D. Ouyang, M. Chen, Q. Huang, J. Weng, Z. Wang, J. Wang, A review on the thermal hazards of the lithium-ion battery and the corresponding countermeasures, Appl. Sci. 9 (2019) 2483, https://doi.org/10.3390/app9122483.
- [46] B. Flamme, J. Światowska, M. Haddad, P. Phansavath, V. Ratovelomanana-Vidal, A. Chagnes, Sulfone-based electrolytes for lithium-ion batteries: cycling performances and passivation layer quality of graphite and LiNi<sub>1/3</sub>Mn<sub>1/3</sub>Co<sub>1/3</sub>O<sub>2</sub> electrodes, J. Electrochem. Soc. 167 (2020) 070508, https://doi.org/10.1149/1945-7111/ab63c3
- [47] G.-Y. Kim, J.R. Dahn, The effect of some nitriles as electrolyte additives in Li-ion batteries, J. Electrochem. Soc. 162 (2015) A437, https://doi.org/10.1149/2.0651503jes.
- [48] K. Liu, F. Ding, J. Liu, Q. Zhang, X. Liu, J. Zhang, Q. Xu, A cross-linking succinonitrile-based composite polymer electrolyte with uniformly dispersed vinyl-functionalized SiO<sub>2</sub> particles for li-ion batteries, ACS Appl. Mater. Interfaces 8 (2016) 23668, https://doi.org/10.1021/acsami.6b05882.
- [49] L. Xia, S. Lee, Y. Jiang, S. Li, Z. Liu, L. Yu, D. Hu, S. Wang, Y. Liu, G.Z. Chen, Physicochemical and electrochemical properties of 1,1,2,2-tetrafluoroethyl-2,2,3,3-tetrafluoropropyl ether as a co-solvent for high-voltage lithium-ion electrolytes. Chemelectrochem 6 (2019) 3747, https://doi.org/10.1002/celc.201900729.
- [50] Y. Gu, S. Fang, L. Yang, S. Hirano, A safe electrolyte for high-performance lithium-ion batteries containing lithium difluoro(oxalato)borate, gamma-butyrolactone and non-flammable hydrofluoroether, Electrochim. Acta 394 (2021) 139120, https://doi.org/10.1016/j.electacta.2021.139120.

[51] H.N. Kim, T. Yim 1, 1,2,2-Tetrafluoroethyl-2,2,3,3-tetrafluoropropyl ether as an advanced electrolyte additive for SiO-based lithium-ion batteries, J. Alloys Compd. 931 (2023) 167529, https://doi.org/10.1016/j.jallcom.2022.167529.

- [52] W.W.A. van Ekeren, M. Albuquerque, G. Ek, R. Mogensen, W.R. Brant, L.T. Costa, D. Brandell, R. Younesi, A comparative analysis of the influence of hydrofluoroethers as diluents on solvation structure and electrochemical performance in non-flammable electrolytes, J. Mater. Chem. A. 11 (2023) 4111, https://doi.org/10.1039/D2TA08404J.
- [53] A.V. Shelkea, J.E.H. Buston, J. Gill, D. Howard, R.C.E. Williams, E. Read, A. Abaza, B. Cooper, P. Richards, J.X. Wen, Combined numerical and experimental studies of 21700 lithium-ion battery thermal runaway induced by different thermal abuse, Int. J. Heat Mass Transf. 194 (2022) 123099, https://doi.org/10.1016/j.ijheatmasstransfer.2022.123099.
- [54] C.H. Doh, Y.C. Ha, S. wook Eom, Entropy measurement of a large format lithium ion battery and its application to calculate heat generation, Electrochim. Acta 309 (2019) 382, https://doi.org/10.1016/j.electacta.2019.04.026.
- [55] S.S. Zhang, K. Xu, T.R. Jow, A thermal stabilizer for LiPF<sub>6</sub>-based electrolytes of Li-ion cells, Electrochem. Solid State Lett. 5 (2002) A206, https://doi.org/
- [56] H.M. Barkholtz, Y. Preger, S. Ivanov, J. Langendorf, L. Torres-Castro, J. Lamb, B. Chalamala, S.R. Ferreira, Multi-scale thermal stability study of commercial lithium-ion batteries as a function of cathode chemistry and state-of-charge, J. Power Sources 435 (2019) 226777, https://doi.org/10.1016/j.ionwsour.2019.226777
- [57] Y.-P. Yang, A.-C. Huang, Y. Tang, Y.-C. Liu, Z.-H. Wu, H.-L. Zhou, Z.-P. Li, C.-M. Shu, J.-C. Jiang, Z.-X. Xing, Thermal stability analysis of lithium-ion battery electrolytes based on lithium bis(trifluoromethanesulfonyl)imide-lithium difluoro(oxalato)borate dual-salt, Polymers 13 (2021) 707, https://doi.org/10.3390/polym13050707.